

Quantization and interference of a quantum billiard with fourfold rotational symmetryZi-Yuan Li  and Liang Huang ^{*}*School of Physical Science and Technology, and Key Laboratory for Magnetism and Magnetic Materials of MOE, Lanzhou University, Lanzhou, Gansu 730000, China*

(Received 12 January 2020; revised manuscript received 30 April 2020; accepted 11 May 2020; published 1 June 2020)

Systems with discrete symmetries are highly important in quantum mechanics. We consider a two-dimensional quantum billiard with fourfold rotational symmetry, where the eigenenergies and eigenstates can be grouped into four symmetry subspaces. Unlike the threefold rotational symmetry case, here the interference of the scarring states on the fundamental domain orbits (FDO) is clean, that they either interfere constructively or annihilate completely. We shall show the complex behavior of the interference revealed in the length spectra for eigenenergies that belong to a particular symmetry subspace and combinations of different symmetry subspaces. We then provide detailed analysis of phase accumulation along the FDOs, which are the keys to determine the interference and could explain the enhancement or annihilation of the peaks well. The quantization condition for the scarring states belonging to different symmetry subspaces is discussed and used to reveal the time-reversal symmetry broken for a particular subspace. An experimental scheme to observe such complex behaviors is also proposed.

DOI: [10.1103/PhysRevE.101.062201](https://doi.org/10.1103/PhysRevE.101.062201)**I. INTRODUCTION**

Quantum systems with discrete symmetry have been an interesting subject in recent years. Any point in the system will be mapped to different images by the operation of the group representing the symmetry, yielding a series of symmetric points. A fundamental domain (FD) is a neighborhood in the original system that contains exactly only one image for any point in the system. Besides the boundary of the whole system, there are additional “boundaries” between adjacent FDs, which are the symmetry lines. Classically, for such a system the ray dynamics can always be reduced to a FD by assuming specular reflections at the symmetry lines [1], where a complete periodic orbit of the original system reduces to a fundamental domain orbit (FDO) that resides completely within an FD. The wave functions of the system can be grouped into different symmetry subspaces according to the discrete symmetry of the original system, and they will follow different constraints on the symmetry lines of the FD depending on which symmetry subspace they belong to.

One intriguing point for the discrete rotational symmetric billiards is that although the whole system may preserve the time-reversal (T-) symmetry, a particular symmetry subspace could violate the T-symmetry and could be revealed in spectral statistics. In general, the spectral fluctuation properties in quantum billiards with chaotic classical dynamics can be described by the random matrix theory [2–5], for those that keep T-symmetry and no other symmetries, the spectral statistics follow the Gaussian orthogonal ensemble (GOE) statistics. If the T-symmetry is broken, then it will follow Gaussian unitary ensemble (GUE), where typically an external magnetic field is needed [6]. The T-symmetry broken and GUE statistics or

partial T-symmetry broken have been observed in microwave experiments [7–12]. Other cases that break T-symmetry and could yield GUE statistics include the massless or massive Dirac billiards due to the boundary condition [13–18], a subset of eigenstates that are localized in a particular region in phase space [19–23], etc.

In 1996, a numerical finding by Leyvraz *et al.* in a quantum billiard with threefold rotational symmetry revealed that the system has the Kramers doublets and one singlet belonging to different symmetry subspaces, which can show GUE and GOE statistics, respectively [24]. Microwave billiard experiments simulating such a quantum billiard was investigated in 2000 by Dembowski *et al.* [25] using superconducting microwave cavities, where the doublets can be identified by small splittings in the spectrum peaks caused by mechanical imperfections of the cavity and the perturbative influences of the antennas. The GUE statistics was confirmed by using only the doublets. A transition from GOE to GUE in a microwave billiard with threefold rotational symmetry was also observed in 2002 [26]. A follow-up experiment in 2003 [27] provided an updated method by modifying the phase difference of the two input antennas locating on the symmetric points to identify the symmetry subspace that an eigenstate belongs. The semiclassical evaluation of the two-point correlation function was applied to understand the spectral properties of the symmetry subspaces, which fully agrees with the predictions of RMT [28].

In line with the development of the semiclassical theory of quantum spectral density in terms of the periodic orbits [29–34], the semiclassical treatment of quantum billiards with discrete symmetries was also considered [35,36], where the FDOs play an important role in shaping the spectral fluctuation properties. Particularly, the form of the symmetry-projected Green’s function was derived by Robbins [35] in 1989 with weights determined by the characters of the

^{*}huangl@lzu.edu.cn

symmetry group. It has been proved that if one sums over all the symmetry-projected Green's functions, the Gutzwiller's trace formula will be recovered. The systems with discrete symmetry like the Sinai billiard, the stadium billiard, a particle in a periodic potential and certain crystals with rotational symmetry were discussed [35]. A group-theoretical analysis was applied by Seligman and Weidenmüller in 1994 to clarify the structure of the periodic orbits in the configuration space of a system with discrete symmetry, and the sum over the periodic orbits was modified to a sum of contributions over classes [37]. In 1997, Keating and Robbins [38] semiclassically explained the de-symmetrized spectra properties of the fold symmetry billiards, where the phase factors in the reduced trace formula with the example of a quantum billiard with threefold rotational symmetry was analyzed.

Here in this work, by investigating a quantum billiard with fourfold rotational symmetry, we shall show vivid examples of quantization on the FDOs and their complex interference effects in shaping the spectral fluctuations. After grouping the eigenstates into different symmetry subspaces, the scarring states [39–41] are identified, which localize particularly along the classically *unstable* periodic orbits [41], in contrast to the classical counterpart where the probability for a particle to travel along the unstable periodic orbits is zero due to the vanishing measure of these orbits in the phase space. Recent progresses include relativistic quantum scars [14–16,42–45], scars in the two-dimensional harmonic oscillators induced by local impurities [46–49], quantum many-body scars that lead to the weak ergodicity breaking [50–56], etc. Particularly, statistics of scars on the FDOs in the $m = 1$ symmetry subspace will be carried out and demonstrated T-symmetry violation. The constructive or destructive interference either for forward and backward orbits inside a symmetry subspace or for mixing different symmetry subspaces will be analyzed in details for different FDOs. Unlike that in the threefold rotational symmetry billiard, where the interference can not be completely enhanced or annihilated (see more details in the Appendix), here it has perfect enhancement or annihilations, thus in the length spectra, some peaks only appear in certain symmetry subspaces or certain mixing of different symmetry subspaces, while some other peaks appear only in other situations. We shall carry out detailed phase analysis for the FDOs and give their quantization conditions, with which the enhancement or complete cancellation can be explained precisely.

It should be noted that in Ref. [57], Robinett considered the length spectra of “folded” versions of the standard circular and square quantum billiards, e.g., half-circle billiard, quarter-circle billiard, etc., and identified peaks corresponding to orbits in the “folded” billiards, that not found in the length spectrum of the full billiard. In his treatment, each folded billiard is itself a complete billiard, i.e., satisfying the Dirichlet boundary condition along all the boundaries including the symmetry lines. Therefore, it is not a symmetry subspace of the original full billiard and interference between different symmetry subspaces was not a concern in his study.

In Sec. II we choose a conformal map to obtain the fourfold rotational symmetry billiard with chaotic dynamics, and solve the Schrödinger equation on this domain. We describe briefly the method that how to obtain the solutions

in different symmetry subspaces and discuss the symmetry properties for the wave functions. In Sec. III we carry out extensive numerical investigations on the spectral properties in different symmetry subspaces, including spectral statistics and comparison with random matrix theory, length spectra for each single symmetry subspace and combinations of any two symmetry subspaces, etc. Furthermore, we will show detailed analysis of how the different types of orbits are influenced by the phase constrains, e.g., their quantization conditions for different symmetry subspaces, and how they interference constructively or destructively depending on their phase relations and symmetry subspaces. The analysis explains the numerical length spectra peaks perfectly. Section IV shows the scar statistics of the $m = 1$ symmetry subspace and demonstrates T-symmetry violation. Possible experimental schemes are discussed in Sec. V. Generalization to M -fold rotational symmetry quantum billiard is discussed in Sec. VI. Conclusions are presented in Sec. VII. As a comparison, the length spectra for a threefold rotational symmetry quantum billiard are presented in the Appendix.

II. METHOD

A. The quantum billiard with fourfold rotational symmetry

We consider a quantum billiard, i.e., a particle that moves freely inside a plane domain D and reflects specularly at the boundary, described by the Hamiltonian

$$\hat{H} = -\frac{\hbar^2}{2m}\nabla^2 + V(\mathbf{r}), \quad (1)$$

where $V(\mathbf{r}) = 0$ inside D and $V(\mathbf{r}) = \infty$ otherwise. This leads to the eigenproblem

$$-\frac{\hbar^2}{2m}\nabla^2\psi(\mathbf{r}) = E\psi(\mathbf{r}), \quad (2)$$

with Dirichlet boundary condition

$$\psi(\mathbf{r})|_{\partial D} = 0, \quad (3)$$

where $E = \hbar^2 k^2 / (2m)$, yielding a set of eigenenergies E_n (or eigenwave numbers k_n) and eigenwave functions $\psi_n(\mathbf{r})$. The domain D can be constructed from the unit disk in the z plane as

$$w = [z(1 + 0.075z^4 + 0.075e^{i\frac{\pi}{2}}z^8)] \times R, \quad (4)$$

where R is the scale of the system, and the unit disk is given by

$$z = \rho \exp(i\phi), \quad \rho \in [0, 1] \text{ and } \phi \in [0, 2\pi].$$

The domain described by Eq. (4) has fourfold rotational symmetry, e.g., see Fig. 1(a).

The position \mathbf{r} in the w plane can be expressed as $[x, y] = [\Re(w), \Im(w)]$, or $\mathbf{r} = [|w|, \arg(z)] = (r, \theta)$ in polar coordinates, where r and θ are functions of (ρ, ϕ) . The boundary of the billiard is given by Eq. (4) when $\rho = 1$. Note that the system defined in this way has a smooth boundary with the desired symmetry. Furthermore, it allows the conformal mapping method to solve the Helmholtz equation in this domain, by transforming back to the unit disk, as detailed in the next subsection.

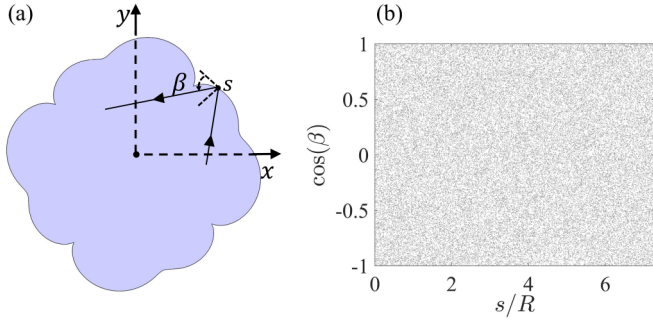


FIG. 1. (a) A sketch of the two-dimensional billiard region D given by Eq. (4). The fourfold rotational symmetry is apparent. The region bordered by the x and y axis forms a FD of the system. (b) The Poincaré section of the classical ray dynamics with 500 000 collision points. $\beta \in (0, \pi)$ is the angle between the outgoing trajectory and the tangential direction of the boundary at the colliding point, s is the arc length along the boundary starting from the positive x axis and indicates the position of colliding point.

The classical ray dynamics of the billiard with such a boundary is chaotic, as evidenced by the Poincaré section in Fig. 1(b). In addition, the Lyapunov exponent of the ray dynamics has also been calculated and confirmed to be positive.

For this fourfold rotational symmetric quantum billiard, the Hamiltonian is invariant under the $\frac{\pi}{2}$ rotation operation \mathcal{R} , i.e., $[\mathcal{R}, \hat{H}] = 0$, the eigenfunctions of \hat{H} can be chosen as eigenfunctions of \mathcal{R} , i.e.,

$$\begin{aligned} \psi_n^{(m)}\left(r, \theta + \frac{\pi}{2}\right) &= \mathcal{R}\psi_n^{(m)}(r, \theta) \\ &= \exp\left(im\frac{\pi}{2}\right)\psi_n^{(m)}(r, \theta), \end{aligned} \quad (5)$$

where $m = 0, 1, 2, 3$. Thus, these eigenfunctions and their corresponding eigenenergies $E_n^{(m)}$ can be grouped into four classes, as will be denoted by the superscript m . In addition, assume that $\psi^{(m)}$ is an eigenfunction of \mathcal{R} that $\mathcal{R}\psi^{(m)} = \exp(im\frac{\pi}{2})\psi^{(m)}$, then when $m_i \neq m_j$,

$$\begin{aligned} \langle \psi^{(m_i)} | \mathcal{R}\hat{H} - \hat{H}\mathcal{R} | \psi^{(m_j)} \rangle \\ = \left[\exp\left(im_i\frac{\pi}{2}\right) - \exp\left(im_j\frac{\pi}{2}\right) \right] \langle \psi^{(m_i)} | \hat{H} | \psi^{(m_j)} \rangle = 0. \end{aligned}$$

This indicates that $\langle \psi^{(m_i)} | \hat{H} | \psi^{(m_j)} \rangle = 0$, and the Hamiltonian can be reduced into four independent blocks, i.e., $\hat{H} = \text{diag}[\hat{H}^{(0)}, \hat{H}^{(1)}, \hat{H}^{(2)}, \hat{H}^{(3)}]$. Thus, $\psi_n^{(m)}$ and $E_n^{(m)}$ are actually eigenstates and eigenenergies of $\hat{H}^{(m)}$.

The system also holds the time-reversal symmetry \mathcal{T} , which can be represented as the conjugate operator \mathcal{K} . We have $\mathcal{T}|\psi_n^{(0)}\rangle = |\psi_n^{(0)}\rangle$, $\mathcal{T}|\psi_n^{(2)}\rangle = |\psi_n^{(2)}\rangle$, and $\mathcal{T}|\psi_n^{(1)}\rangle = |\psi_n^{(3)}\rangle$. Thus, $E_n^{(1)}$ and $E_n^{(3)}$ form Kramers doublets, while $E_n^{(0)}$ and $E_n^{(2)}$ are singlets.

B. Conformal mapping method to solve the system

To solve the eigenequation Eq. (2) with the Dirichlet boundary condition Eq. (3) on the chaotic domain D , we employ the conformal mapping method [6,58–60], and transform the problem to a modified equation with also the Dirichlet boundary condition but on the unit disk in

the $z = (\rho, \phi)$ plane. Furthermore, the functions satisfying the Dirichlet boundary condition on the unit disk form a Hilbert space, and one particular orthonormal basis is given by the eigensolutions of the Helmholtz equation on the unit disk, i.e., $\{\bar{\psi}_{l,q}(\rho, \phi) = \bar{N}_{l,q} \exp(il\phi) J_l(\mu_{l,q}\rho), l = \dots, -1, 0, 1, \dots; q = 1, 2, 3, \dots\}$, as guaranteed by the Sturm-Liouville eigenvalue problems, where $\bar{N}_{l,q} = [2\pi \int_0^1 d\rho \rho J_l^2(\mu_{l,q}\rho)]^{-1/2}$ is the normalization constant, $J_l(\mu_{l,q}\rho)$ is the Bessel function, and $\mu_{l,q}$ is the q th zero of J_l .

With the function $w(z)$ being analytic, $\nabla_w^2 = \nabla_z^2 / |dw/dz|^2$, and $\psi(\mathbf{r}) = \psi[w(z)] = \psi(z)$, Eq. (2) becomes

$$-\frac{\hbar^2}{2m} \frac{1}{|dw/dz|^2} \nabla_z^2 \psi(z) = E \psi(z). \quad (6)$$

$\psi(z)$ can be expanded on the basis of $\{\bar{\psi}_{l,q}\}$,

$$\psi(\rho, \phi) = \sum_{l,q} c_{l,q} \bar{\psi}_{l,q}(\rho, \phi). \quad (7)$$

Once the coefficients $c_{l,q}$ are determined, the eigenfunction of the original billiard D is obtained. In principle, the summation is over an infinite number of terms, but practically, the basis needs to be truncated to make the problem numerically solvable, and we choose the first 40 000 eigensolutions in the increasing order of $\mu_{l,q}$. Substituting the expansion Eq. (7) back to Eq. (6), and using the orthogonal relation of the basis, one gets

$$\frac{v_{l,q}}{k^2} - \sum_{l',q'} M_{l,q;l',q'} v_{l',q'} = 0, \quad (8)$$

where $k^2 = 2mE^2/\hbar^2$, $v_{l,q} = \mu_{l,q} c_{l,q}$ and

$$\begin{aligned} M_{l,q;l',q'} &= \frac{N_{l',q'} N_{l,q}}{\mu_{l',q'} \mu_{l,q}} \int_0^{2\pi} d\phi \exp[i(l' - l)\phi] \\ &\times \int_0^1 d\rho \rho T(\rho, \phi) J_l(\mu_{l,q}\rho) J_{l'}(\mu_{l',q'}\rho), \end{aligned} \quad (9)$$

where $T(\rho, \phi) = |dw/dz|^2$. Once the matrix elements $\{M_{l,q;l',q'}\}$ are obtained, one can solve the eigenproblem $M\mathbf{v} = \lambda\mathbf{v}$ with a set of eigenvalues and eigenvectors $\{\lambda_n, \mathbf{v}^n, n = 1, 2, \dots\}$. Then the expanding coefficients in Eq. (7) are given by $c_{l,q}^n = v_{l,q}^n / \mu_{l,q}$, thus $\psi_n(\rho, \phi) = \sum_{l,q} v_{l,q}^n \bar{\psi}_{l,q} / \mu_{l,q}$. The eigenvalue number is given by $k_n = 1/\sqrt{\lambda_n R}$, or $E_n = \hbar^2/2m\lambda_n R^2$. This yields the eigenenergies E_n and eigenwave functions $\psi_n(\mathbf{r})$ of the original billiard [Eqs. (2) and (3)].

Furthermore, since the system has the fourfold rotational symmetry and the basis function $\bar{\psi}_{l,q}$ can also be grouped into four classes based on the values of l , the above solving procedure can be grouped by summing l selectively depending on m in the expansion Eq. (7):

$$\psi^{(m)} = \sum_{l_m,q} c_{l_m,q} \bar{\psi}_{l_m,q}, \quad (10)$$

where $l_m = 4p + m$, $p = 0, \pm 1, \pm 2, \dots$. The resulting eigenwave function $\psi_n^{(m)}$ will then belong to the same class of m with eigenenergy $E_n^{(m)}$. It is clear that the eigenwave function $\psi_n^{(m)}$ and eigenenergy $E_n^{(m)}$ of the Hamiltonian Eq. (1) in class m defined by Eq. (5) can be regarded as eigensolutions of Eqs. (2) and (3) on the FD of the system, i.e., for any θ_0 ,

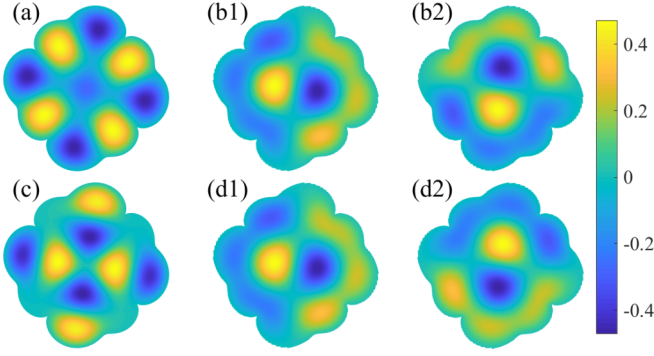


FIG. 2. Typical examples of wave functions revealing the corresponding symmetry. (a–d) The third eigenfunction in $\hat{H}^{(0)}$, $\hat{H}^{(1)}$, $\hat{H}^{(2)}$, and $\hat{H}^{(3)}$, respectively. (b1, b2) and (d1, d2) are the real and imaginary parts of the third eigenfunction of $\hat{H}^{(1)}$ and $\hat{H}^{(3)}$, respectively.

the region defined by $\theta \in [\theta_0, \theta_0 + \pi/2]$ in D , with additional “boundary conditions” along θ_0 and $\theta_0 + \pi/2$ following the same constraint Eq. (5):

$$\begin{aligned} \psi_n^{(m)}\left(r, \theta_0 + \frac{\pi}{2}\right) &= \mathcal{R}\psi_n^{(m)}(r, \theta_0) \\ &= \exp\left(im\frac{\pi}{2}\right)\psi_n^{(m)}(r, \theta_0). \end{aligned} \quad (11)$$

In return, the wave function in this subdomain can be used to generate the wave function for the whole billiard domain D by applying \mathcal{R} repeatedly to get the wave functions on the regions $[\theta_0 + \pi/2, \theta_0 + \pi]$, $[\theta_0 + \pi, \theta_0 + 3\pi/2]$, and $[\theta_0 + 3\pi/2, \theta_0 + 2\pi]$ and then gluing them together.

Figure 2 shows representative wave functions belonging to different symmetry subspaces. According to Eq. (5), for $m = 0$, after rotating $\pi/2$, the wave function returns to itself, as exemplified in Fig. 2(a). For $m = 1$, $\psi_n^{(m)}(r, \theta + \frac{\pi}{2}) =$

$i\psi_n^{(m)}(r, \theta)$, thus after rotating $\pi/2$ the real part becomes the imaginary part, and the imaginary part becomes negative of the real part, which is clear in Fig. 2(b). For $m = 2$, after rotating $\pi/2$, $\psi_n^{(m)}(r, \theta + \frac{\pi}{2}) = -\psi_n^{(m)}(r, \theta)$, thus maximum becomes minimum, and vice versa, as shown in Fig. 2(c). For $m = 3$, $\psi_n^{(m)}(r, \theta + \frac{\pi}{2}) = -i\psi_n^{(m)}(r, \theta)$, i.e., the real part becomes negative of the imaginary part, while the imaginary part becomes the real part, as demonstrated in Fig. 2(d).

Figure 3 shows the spectra statistics. To remove the nonuniform effect of the density of energy levels in the spacing statistics, for a given set of energy levels, e.g., those for a particular symmetry subspace, or a mixing of two symmetry subspaces, the number of levels $N(E)$ below E and its smooth part $\langle N(E) \rangle$ are obtained. For each eigenenergy E_n , define $x_n \equiv \langle N(E_n) \rangle$, the unfolded nearest-neighbor spacing is then $S_n = x_{n+1} - x_n$. The such obtained distribution $P(S)$ of S_n yields $\int P(S)SdS = 1$ automatically, i.e., S_n is normalized with average value of 1 irrespective to system details. Typically, for two-dimensional quantum billiards with Dirichlet boundary condition, the smooth part $\langle N(E) \rangle$ can be given by the Weyl formula,

$$\langle N(E) \rangle = \frac{mAE}{2\pi\hbar^2} - \frac{L}{2\pi}\sqrt{\frac{2mE}{\hbar^2}},$$

where A is the area and L is the perimeter of the billiard. While for more complex situations, the second term could be modified. Therefore, for the symmetry subspace, as the boundary condition on the symmetry line is neither Dirichlet or Neumann, we use a smooth fitting to $N(E)$ to get $\langle N(E) \rangle$, which is close to the Weyl formula. Figure 3(a) is the level spacing statistics for all the levels. Note that due to degeneracy of $E_n^{(1)}$ and $E_n^{(3)}$, only $E_n^{(1)}$ s are included. Figures 3(b)–3(d) show the level spacing statistics for $E_n^{(0)}$, $E_n^{(1)}$, and $E_n^{(2)}$, respectively. According to the Bohigas-Giannoni-Schmit (BGS) conjecture [2], due to the classically chaotic dynamics, the

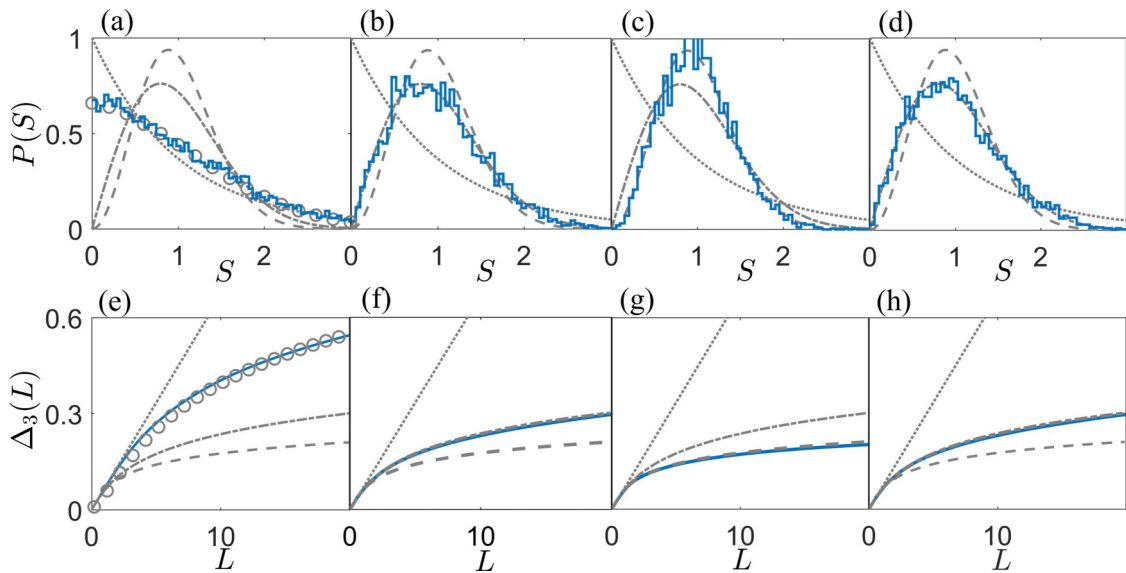


FIG. 3. (a–d) The nearest-neighbor spacing distribution $P(S)$ (solid staircase curves) for all the energy levels (a) and for symmetry subspaces $\hat{H}^{(0)}$ (b), $\hat{H}^{(1)}$ (c), and $\hat{H}^{(2)}$ (d), respectively. (e–h) The corresponding Dyson-Metha Δ_3 statistics. The dotted, dash-dotted, and dashed lines are the theoretical curves for Poisson, GOE and GUE distributions. Circles in (a) and (e) are random matrix results with two GOE ensembles and one GUE ensemble.

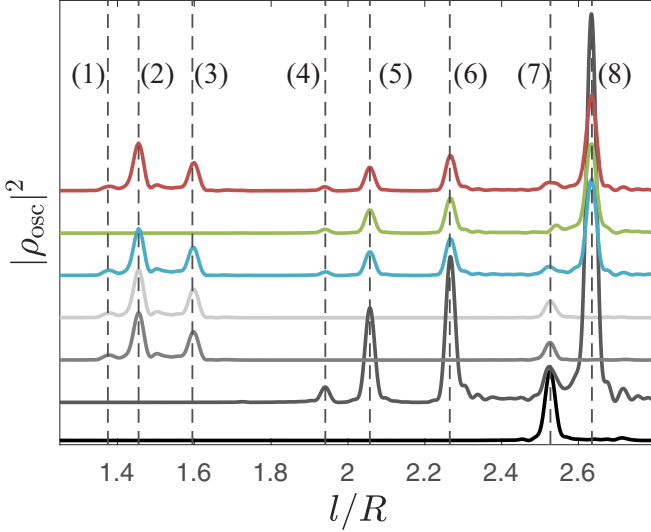


FIG. 4. From top to bottom, the length spectra for energy levels belongs to $\hat{H}^{(0)}$, $\hat{H}^{(1)}$, and $\hat{H}^{(2)}$, and mixing of symmetry subspaces $\hat{H}^{(0,1)}$, $\hat{H}^{(1,2)}$, and $\hat{H}^{(0,2)}$, and the one for the whole system. The labels from (1) to (8) correspond to the different types of orbits shown in Fig. 5. The same set of energy levels as in Fig. 3 are used here, and the corresponding wave vector $|\mathbf{k}|$ is up to $241.3/R$.

level spacing statistics are GOE, GUE, and GOE, respectively, for these three subspaces. The GUE statistics for the $E_n^{(1)}$'s are due to the Kramers degeneracy, that when considering only a single subspace, it breaks the time-reversal symmetry [24]. Note that in Fig. 3(a) the random matrix simulation results with two GOE ensemble and one GUE ensemble are also presented as the circles, which agree with the results of the system well. $\Delta_3(L)$ for these cases are shown in Figs. 3(e)–3(h), and the results agree with the $P(S)$ well.

III. LENGTH SPECTRA ANALYSIS

A convenient tool to reveal the signatures of classical periodic orbits is the length spectrum [61–63]. Once the eigenenergies are obtained, the fluctuation part of the density of states $\rho_{\text{osc}}^{(m)}(k)$ for each symmetry subspace m can be extracted, and the length spectra $\rho_{\text{osc}}^{(m)}(l)$ can be obtained from $\rho_{\text{osc}}^{(m)}(k)$ by a Fourier transform,

$$\rho_{\text{osc}}^{(m)}(l) = \int_k dk \rho_{\text{osc}}^{(m)}(k) \exp(ikl). \quad (12)$$

Figure 4 shows the length spectra from energy levels belongs to different symmetry subspaces and their combinations. Since our focus is the FDOs, the range of the length is chosen only in a window containing the most dominating FDOs. The peaks in this figure all correspond to the orbits within a FD, as shown in Fig. 5. Note that the length spectra peaks for different symmetry subspaces are quite different. For example, the peaks (1–3) are presented in $\rho_{\text{osc}}^{(m)}(l)$ for $\hat{H}^{(0)}$ and $\hat{H}^{(2)}$, but disappeared for $\hat{H}^{(1)}$. The behaviors are even more complicated when combining energy levels from two different symmetry subspaces. For example, when mixing $\hat{H}^{(0)}$ and $\hat{H}^{(1)}$, or $\hat{H}^{(2)}$ and $\hat{H}^{(1)}$, the peaks (4–6) and (8) are annihilated completely; but when mixing $\hat{H}^{(0)}$ and $\hat{H}^{(2)}$, the

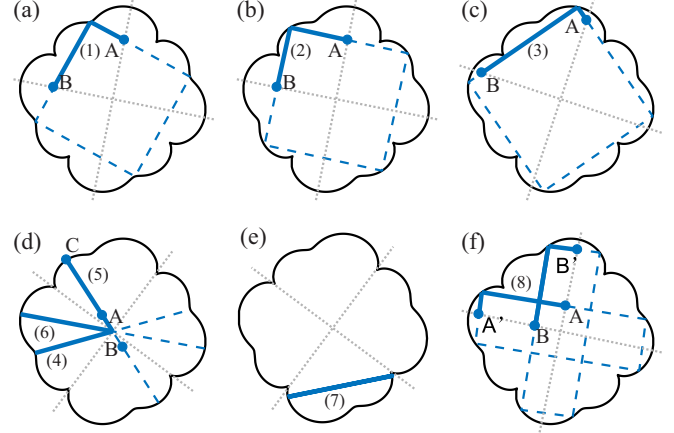


FIG. 5. The FDOs that are revealed by the peaks of Fig. 4. The neighboring dotted lines enclose the FD, i.e., a quarter of the full billiard. (a, b, c) The FDOs (1), (2), and (3), i.e., one-fourth of a square. (d) The FDOs (4, 5, 6) of bouncing ball orbits that form a cross as rotating $\pi/2$ will be also a solution of the system. (e) The bouncing ball orbit (7) that resides completely inside a FD. (f) The FDO (8) of a parallelogram orbit. We denote l as the length of FDOs and L as the length of the complete orbits. T is the number of reflections at the actual boundary of the full billiard of the complete orbits. Then for these orbits: (1) $T = 4$, $L = 5.5R$, and $l = L/4$; (2) $T = 4$, $L = 5.815R$, and $l = L/4$; (3) $T = 4$, $L = 6.405R$, and $l = L/4$; (4) $T = 2$, $L = 3.895R$, and $l = L/2$; (5) $T = 2$, $L = 4.113R$, and $l = L/2$; (6) $T = 2$, $L = 4.529R$, and $l = L/2$; (7) $T = 2$, $L = 2.528R$, and $l = L$; (8) $T = 4$, $L = 5.269R$, and $l = L/2$.

peaks (4–6) and (8) are enhanced, while the peaks (1–3) are annihilated. When combining all the energy levels together, all the peaks are annihilated in the length spectra plot, except that marked by (7), which is an orbit in the FD, but also a complete orbit of the original billiard without intersecting the symmetry lines defining the FD. Note that the symmetry line $\theta = \theta_0$ of the FD can be chosen arbitrarily for analyzing different orbits.

To examine the eigenstates for different symmetry subspaces, scarring patterns on classical orbits are identified and analyzed. To explain the features observed in the length spectra, we examine the quantization condition of the states along the FDOs, particularly by analyzing the phase accumulations along these FDOs. It should be noted that the appearance of the periodic orbits in the length spectra does not depend on the existence of strongly scarred states. In particular, the width of the scars goes to zero in the semiclassical limit [41,64,65], whereas the height of the peaks for the isolated unstable periodic orbits are constant (independent of k) in the trace formula. However, the recurrence of the scars following the quantization condition of the action exerts a periodic modulation of the density of states, resulting in the peaks in the length spectra.

A. Square orbits

For state $\psi_j^{(m)}$ of a particular symmetry subspace m , the quantization rule can be summarized as follows. Let us consider a type of square orbits shown in Figs. 5(a)–5(c). The FDO contains one-fourth of the complete orbit, with two ends marked by A and B that $w(B) = iw(A)$ or $\theta(B) = \theta(A) +$

$\pi/2$. The boundary condition for the two straight symmetry lines due to the discrete rotational symmetry are given by

$$\psi_j^{(m)}|_B = \exp(im\pi/2)\psi_j^{(m)}|_A \quad (13)$$

or

$$\psi_j^{(m)}|_A = \exp(-im\pi/2)\psi_j^{(m)}|_B. \quad (14)$$

However, in the semiclassical scheme, the accumulated phase for a particle traveling from A to B along the FDO is given by

$$\psi_j^{(m)}|_B = \exp\left[i\left(kl + N\frac{\pi}{2}\right)\right]\psi_j^{(m)}|_A, \quad (15)$$

where k is the wave number, l is the length of the FDO, $N = 1$ is the number of reflections at the actual boundary of the full billiard for the FDO, and $\pi/2$ is the contribution of each reflection including the effects of the reflection coefficient ($-\pi$) and the conjugate point ($-\pi/2$). Note that in general the effects of the reflection coefficients and the conjugate points are separate, but for the shape of the billiard, there will be a conjugate point after each reflection at the boundary of the full billiard, therefore they always show up together, and it would be convenient to write them together as $-3\pi/2 = \pi/2 \bmod 2\pi$. Considering that the particle travels from A to B along the FDO and then teleports back to A via the boundary condition (14), the new wave function at A is given by

$$\begin{aligned} \tilde{\psi}_j^{(m)}|_A &= \exp(-im\pi/2) \exp\left[i\left(kl + N\frac{\pi}{2}\right)\right]\psi_j^{(m)}|_A \\ &= \exp(i\Phi^+)\psi_j^{(m)}|_A, \end{aligned} \quad (16)$$

with

$$\Phi^+ = -m\pi/2 + \left(kl + N\frac{\pi}{2}\right). \quad (17)$$

The quantization condition for a scar to possibly appear is that such obtained wave function at A must equal to its original value, $\tilde{\psi}_j^{(m)}|_A = \psi_j^{(m)}|_A$, or the phase Φ^+ must be an integer multiple of 2π : $\Phi^+ = 2n\pi$.

If the particle travels along the FDO reversely from B to A and then back to B via the boundary condition Eq. (13), then one has

$$\begin{aligned} \tilde{\psi}_j^{(m)}|_B &= \exp(im\pi/2) \cdot \exp\left(i\left(kl + N\frac{\pi}{2}\right)\right)\psi_j^{(m)}|_B \\ &= \exp(i\Phi^-)\psi_j^{(m)}|_B, \end{aligned} \quad (18)$$

thus

$$\Phi^- = m\pi/2 + \left(kl + N\frac{\pi}{2}\right), \quad (19)$$

And the quantization condition for scars to appear is $\Phi^\pm = 2n'\pi$.

Denote $A^\pm(l)$ as the contribution to the length spectra from states along the FDO $A - B - A$ (denoted by “+”) and its reversed counterpart $B - A - B$ (denoted by “-”) of orbital length l . Then we have

$$A^+(l) = e^{i\Delta\Phi}A^-(l), \quad (20)$$

where $\Delta\Phi = \Phi^+ - \Phi^-$ is the difference of the phase accumulation of the particle cycling the complete orbit between “+”

and “-” orientations. For the FDOs shown in Figs. 5(a)–5(c) and Eqs. (17) and (19), one has

$$\Delta\Phi = -m\pi.$$

Note that when calculating $\Delta\Phi$, Φ^+ , and Φ^- do not need to meet the quantization condition that they are integer multiples of 2π . The height of the peak in the length spectrum at length l is

$$\rho_{\text{osc}}(l)^2 \sim |A^+(l) + A^-(l)|^2 = |1 + e^{i\Delta\Phi}|^2 |A^-(l)|^2. \quad (21)$$

Alternatively, $\rho_{\text{osc}}^{(m)}(k)$ can be obtained semiclassically from the symmetry projected trace formula [35,36,38], from which the relative phase of forward and backward orbits can be obtained similarly.

For a particular symmetry subspace m , when $m = 1$ or 3 , $\Delta\Phi = -\pi$ or -3π , then the contributions of the two orientations cancel each other and $\rho_{\text{osc}}(l)^2 = 0$. Note that this indicates the two orientations cannot fulfill the quantization conditions simultaneously for the same k (energy), which breaks the time-reversal symmetry, leading to GUE spectral statistics. While for $m = 0$ or 2 , $\Delta\Phi = 0 \bmod 2\pi$, $\rho_{\text{osc}}(l)^2$ has the maximum value. This is clear in Fig. 4 from the peaks indicated by (1–3), as there are peaks for $m = 0$ and 2 , but $\rho_{\text{osc}}(l)^2$ is completely flat for $m = 1$.

When combining two symmetry subspaces together, for $\hat{H}^{(0)}$ and $\hat{H}^{(1)}$, the peaks (1–3) are the same as that for $\hat{H}^{(0)}$; and for $\hat{H}^{(2)}$ and $\hat{H}^{(1)}$, these peaks are the same as that for $\hat{H}^{(2)}$, as expected. But when combining $\hat{H}^{(0)}$ and $\hat{H}^{(2)}$, to our surprise, these three peaks are disappeared. Heuristically, $\rho_{\text{osc}}(l)^2$ has contributions from four parts in terms of $e^{i\Phi^\pm(m)}$, neglecting the common part of the phases in Eqs. (17) and (19), we have

$$\begin{aligned} \rho_{\text{osc}}(l)^2 &\sim |A_{(m=0)}^+ + A_{(m=0)}^- + A_{(m=2)}^+ + A_{(m=2)}^-|^2 \\ &\sim |1 + 1 + e^{-i\pi} + e^{i\pi}|^2 = 0. \end{aligned}$$

Furthermore, since there are no peaks for $\hat{H}^{(1)}$ and $\hat{H}^{(3)}$, and the peaks for $\hat{H}^{(0)}$ and $\hat{H}^{(2)}$ cancel each other, when combining all the energy levels together, all of the three peaks should disappear, which is indeed the case as shown in the bottom curve of Fig. 4. Actually, all the peaks for the FDOs that under the constraint of Eq. (13) disappear.

B. Cross orbits

For the cross type of orbits, i.e., the orbits (4–6) shown in Fig. 5(d), they are bouncing ball orbits passing the center of the billiard, and unlike orbits (1–3), their time-reversed orbits are identical to themselves. To analyze the phase, we mark three points on the orbit, A , C , and B as indicated in Fig. 5(d), where C is the reflecting point on the billiard boundary, and the two points A and B are *infinitesimally* close to each other but on the two sides of the center. Therefore from B to A the rotational angle is π , and the boundary condition yields

$$\psi_j^{(m)}|_A = \exp(-im\pi)\psi_j^{(m)}|_B. \quad (22)$$

Depending on whether rotating counterclockwise or clockwise, the phase can be $-m\pi$ or $m\pi$, which are equivalent in the analysis. Taking account of the phase accumulation along

the orbit from A to C to B , and since there is only one reflection point, one has

$$\begin{aligned}\tilde{\psi}_j^{(m)}|_A &= \exp(-im\pi) \cdot \exp\left(i\left(kl + \frac{\pi}{2}\right)\right) \psi_j^{(m)}|_A \\ &= \exp(i\Phi^+) \psi_j^{(m)}|_A,\end{aligned}\quad (23)$$

thus

$$\Phi = -m\pi + \left(kl + \frac{\pi}{2}\right).\quad (24)$$

Since the time-reversed orbits are identical to themselves, there will be no destructive interference between the forward and backward orbits for a given symmetry subspace m . Thus, all the symmetry subspaces show these peaks in the length spectrum, i.e.,

$$\rho_{\text{osc}}(l)^2 \sim |A(l)|^2.\quad (25)$$

When combining two symmetry subspaces together, e.g., for $m = 0$ and $m = 1$, from Eq. (24), and neglecting the common part, we have

$$\begin{aligned}\rho_{\text{osc}}(l)^2 &\sim |A_{(m=0)} + A_{(m=1)}|^2 \\ &\sim |1 + e^{-i\pi}|^2 = 0.\end{aligned}$$

Thus, these peaks in the length spectra disappear. Similar situations occur for $m = 1$ and $m = 2$, where these peaks also disappear.

For $m = 0$ and $m = 2$, one has

$$\begin{aligned}\rho_{\text{osc}}(l)^2 &\sim |1 + e^{-i2\pi}|^2 |A^\pm(l)|^2 \\ &= 4|A^\pm(l)|^2.\end{aligned}$$

Thus, the height of the peak is about four times higher than the peaks for a single symmetry subspace. The above analysis explains the relative heights of the peaks in Fig. 4 for (4–6) orbits in the mixing cases well.

C. The bouncing ball orbit within a FD

Orbit (7) is a bouncing ball orbit that resides completely inside a FD without intersections with the symmetry lines, as shown in Fig. 5(e). Thus, the rotational symmetry does not impose any constraint on this orbit, and the total phase accumulation after a complete cycle around the orbit is

$$\Phi^+ = \Phi^- = kl + 2\frac{\pi}{2}.\quad (26)$$

Thus, the peak at the length l of this orbit appear in any symmetry subspace, and also any combination of two symmetry subspaces, with the height of 4 times as that for one symmetry subspace. The peak for this orbit also show in the length spectra for combining all the symmetry subspaces, with the height of 16 times as that for one symmetry subspace.

D. Parallelogram orbit

For the parallelogram orbit shown in Fig. 5(f), a complete orbit in the FD can be $A - A' - B' - B - A$ with its reversed counterpart $B - B' - A' - A - B$. The propagation

of the wave function yields

$$\begin{aligned}\tilde{\psi}_j^{(m)}|_A &= \exp\left[im\left(-\frac{\pi}{2}\right)\right] \exp\left[i\left(kl_{B'B} + \frac{\pi}{2}\right)\right] \\ &\quad \times \exp\left[im\left(-\frac{\pi}{2}\right)\right] \\ &\quad \times \exp\left[i\left(kl_{AA'} + \frac{\pi}{2}\right)\right] \psi_j^{(m)}|_A,\end{aligned}\quad (27)$$

where $l_{AA'}$ and $l_{B'B}$ are the length of the orbit from A to A' and from B' to B . The total length of the FDO is thus $l = l_{AA'} + l_{B'B}$. Thus, the accumulated phase is

$$\Phi^+ = -m\pi + kl + \pi.\quad (28)$$

For the reversed orientation, one has

$$\begin{aligned}\tilde{\psi}_j^{(m)}|_B &= \exp\left[im\left(\frac{\pi}{2}\right)\right] \exp\left[i\left(kl_{A'A} + \frac{\pi}{2}\right)\right] \exp\left[im\left(\frac{\pi}{2}\right)\right] \\ &\quad \times \exp\left[i\left(kl_{BB'} + \frac{\pi}{2}\right)\right] \psi_j^{(m)}|_B,\end{aligned}\quad (29)$$

with

$$\Phi^- = m\pi + kl + \pi\quad (30)$$

and

$$\Delta\Phi = -2m\pi.\quad (31)$$

Comparing with Eq. (24) for the cross orbits, they share similar dependence on m , thus the peaks for a symmetry subspace or for two symmetry subspaces share similar features as that for the cross orbits (4–6), i.e., the peaks appear for each symmetry subspace, cancels completely for the combinations of $\hat{H}^{(0)}$ and $\hat{H}^{(1)}$, and $\hat{H}^{(1)}$ and $\hat{H}^{(2)}$, but four times higher for $\hat{H}^{(0)}$ and $\hat{H}^{(2)}$.

IV. SCARS' STATISTICS

We have checked the obtained eigenstates for each symmetry subspace and identified the scarring states along various FDOs. In general, scars will appear repeatedly following the quantization condition. For example, suppose a scar is identified when $k = k_0$ in Eq. (17) or Eq. (19), such that $\Phi_0^\pm = 2n\pi$. Then as k is varied, when the difference in the wave number k , $\Delta k = k - k_0$, satisfies $\Phi_0^\pm + \Delta kl = 2n'\pi$, where l is the length of the FDO and n' is another integer, the scar could appear again. Note that a scar does not always appear when the quantization condition is satisfied. Therefore, after we identify a set of scars with wave numbers $\{k_n, n = 1, 2, \dots\}$ on a FDO with length l , we can choose a particular one and set its wave number as the reference point k_0 , then calculate

$$\eta_n = \frac{|k_n - k_0|}{\delta k} - \left[\frac{|k_n - k_0|}{\delta k} \right],\quad (32)$$

where $\delta k = 2\pi/l$, and $[x]$ returns the maximum integer less or equal to x . This has been previously proposed in Ref. [14]. For systems with time-reversal symmetry, the scarring states with different orientations on the orbit will satisfy the quantization condition simultaneously, or $\text{mod}(\Delta\Phi, 2\pi) = 0$. In this case, η_n will take values either close to 0 or close to 1. However, when $\text{mod}(\Delta\Phi, 2\pi) \neq 0$, if Φ^+ is an integer multiple of 2π and satisfies the quantization condition, then Φ^- will not [15]. This breaks the time-reversal symmetry as if one orientation

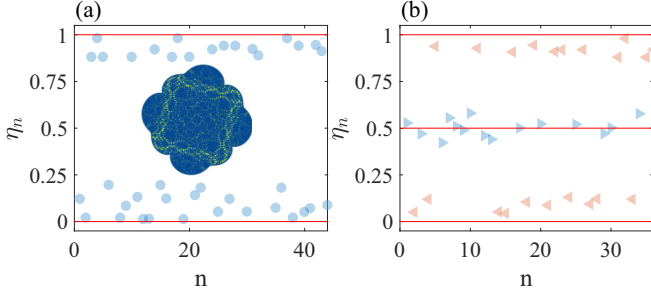


FIG. 6. (a) η_n of scarring states on the square orbit for the symmetry subspace $m = 0$, inset shows an example of the scar which is the 442nd eigenstate in this symmetry subspace. (b) η_n for the symmetry subspace $m = 1$, where left triangles indicate counterclockwise current flow and the right triangles are for the opposite orientation. The reference state has a counterclockwise current flow.

is a solution of the system, then the opposite orientation will be not. In particular, if $\text{mod}(\Delta\Phi, 2\pi) = \pi$, then besides 0 and 1, η_n can also take a value around 0.5. For the four types of orbits that we have analyzed in Sec. III, only the square orbit with $m = 1$ or $m = 3$ breaks the time-reversal symmetry. Since eigenenergies for $\hat{H}^{(1)}$ and $\hat{H}^{(3)}$ are degenerated, we will only focus on $\hat{H}^{(1)}$ and also consider $\hat{H}^{(0)}$ as a comparison. To identify the orientation of the scarring states, we have also calculated the local probability flow $\mathbf{j}(\mathbf{r}) = \frac{1}{2m} [\psi^{(m)*}(\mathbf{r})\hat{P}\psi^{(m)}(\mathbf{r}) - \psi^{(m)}(\mathbf{r})\hat{P}\psi^{(m)*}(\mathbf{r})]$.

Figure 6 shows the results. For each case, we have identified around 40 scarring states. It is clear that for $m = 0$, η_n is either close to 0 or close to 1, but for $m = 1$, η_n takes an extra value of 0.5. In addition, for $m = 1$, the local probability flow of the states is not zero, thus the symbols are distinguished by the flow orientation. As expected, the scarring states with one orientation pertain η_n values of 0 or 1, while for the other orientation $\eta_n \approx 0.5$, indicating a π phase difference.

V. POSSIBLE EXPERIMENTAL SCHEMES

The above results of interference of the eigenstates on the FDOs either within a single symmetry subspace or between different symmetry subspaces can be revealed experimentally by using a superconducting microwave billiard with the same boundary. In microwave billiard experiments, the resonant frequency corresponds to the energy levels of the quantum billiard with the same shape, and the vertical component of the electric field corresponds to the wave function. To do statistics for each symmetry subspace, the eigenfrequencies (eigenenergies) need to be distinguished for different symmetry subspaces. For the ideal fourfold rotational symmetry system, the symmetry subspaces $m = 1$ and $m = 3$ are degenerated, resulting in Kramers doublets. But due to the imperfections in manufacturing the microwave billiard, the degeneracy are typically destroyed, leading to tiny splitting peaks. Since typically neighboring levels that are very close to each other are vary rare due to the level repulsion caused by the chaotic classical dynamics, the doublets (peaks with tiny splittings) can be identified from the other isolated peaks. Thus, the peaks form doublets ($m = 1$ and $m = 3$) and singlets ($m = 0$ and $m = 2$). For the $m = 0$ and $m = 2$ singlets, they

can be distinguished by following a similar method proposed in Ref. [27] for the threefold symmetry billiard. In particular, one can set two input antennas with their positions A and B such that $w(B) = iw(A)$, i.e., rotating A counterclockwise with respect to the center of the billiard by $\pi/2$ will get to B . For $m = 0$, $\psi^{(m)}|_B = \psi^{(m)}|_A$, while for $m = 2$, $\psi^{(m)}|_B = -\psi^{(m)}|_A$. By applying a phase shifter on the input of B , and vary the phase from 0 to π , if a peak belongs to $m = 0$ symmetry subspace, then the peak will change from maximum to minimum, while if the peak belongs to $m = 2$, it will change from minimum to maximum. In this way all the eigenfrequencies can be classified into the different symmetry subspaces, leading to further analysis of interference behavior as revealed in the length spectra plots.

VI. GENERALIZATION TO M-FOLD ROTATIONAL SYMMETRY SYSTEMS

For a system with M -fold rotational symmetry (C_M) with $M > 4$, it is much more complex than a simple generalization of the treatment for the $M = 4$ case, it will depend on the prime factorization of M . For example, if $M = p_1 \times p_2 \times \dots$, then the system also has p_i -fold rotational symmetry. In particular, for classical periodic orbits of the ray dynamics that only has the C_{p_i} symmetry but not the C_M symmetry, the results for p_i -fold rotational symmetry will be applicable for the length spectra peaks of this set of FDOs.

Now assume that M is a prime number or we only consider the C_M orbits, then the wave function satisfies

$$\mathcal{R}\psi^{(m)} = e^{im\frac{2\pi}{M}}\psi^{(m)},$$

where $m = 0, 1, 2, \dots, M - 1$ is the index for the symmetry subspace. Let us consider the length spectrum of the eigenenergies belonging to the subspace m . Consider a periodic orbit that has the C_M symmetry, and assume that the orbit circulates the center of the billiard q times, then for each symmetry subspace m , following similar analysis as in the text, one has $\Delta\Phi = \Phi^+ - \Phi^- = -2qm \cdot 2\pi/M$. Thus, the height of the peak in the length spectrum at the corresponding length l is given by

$$\begin{aligned} \rho_{\text{osc}}(l)^2 &\sim |A^+(l) + A^-(l)|^2 \\ &= |1 + e^{-i2qm2\pi/M}|^2 |A^-(l)|^2, \end{aligned} \quad (33)$$

and whether the interference is constructive or destructive will depend on $4qm/M$. If $4qm/M = 1 \pmod{2}$, then it is completely destructive, and the corresponding peak will not show up in this length spectrum. However, if $4qm/M = 0 \pmod{2}$, then a complete constructive interference will happen, resulting in a big peak. For all other values, partial constructive or destructive interference could be expected.

For mixing of two symmetry subspaces m_1 and m_2 , we have

$$\begin{aligned} \rho_{\text{osc}}(l)^2 &\sim |A_{(m_1)}^+ + A_{(m_1)}^- + A_{(m_2)}^+ + A_{(m_2)}^-|^2 \\ &\sim |e^{-iqm_1 2\pi/M} + e^{iqm_1 2\pi/M} \\ &\quad + e^{-iqm_2 2\pi/M} + e^{iqm_2 2\pi/M}|^2 |A^\pm(l)|^2 \\ &= 4[\cos(2qm_1\pi/M) + \cos(2qm_2\pi/M)]^2 |A^\pm(l)|^2. \end{aligned}$$

Thus, if M is large, then for a given orbit with C_M symmetry and a particular value of q , the dependence of ρ_{osc} on the

values of m_1 and m_2 can be quite complicated. For mixing of b symmetry subspaces, the height of the peak for the FDOs is given by

$$\begin{aligned} \rho_{\text{osc}}(l)^2 &\sim \left| \sum_{j=1}^b (A_{(m_j)}^+ + A_{(m_j)}^-) \right|^2 \\ &\sim \left| \sum_{j=1}^b (e^{-iqm_j 2\pi/M} + e^{iqm_j 2\pi/M}) |A^\pm(l)| \right|^2 \\ &= 4 \left[\sum_{j=1}^b \cos(2qm_j \pi/M) \right]^2 |A^\pm(l)|^2. \end{aligned}$$

The interference among different symmetry subspaces can be completely different for different sets of m_j s.

From these discussions, it is clear that when $M = 4$, for any integer $q > 0$ and m_j , $\cos(2qm_j \pi/M)$ is either zero or ± 1 , thus complete constructive or destructive interference has been observed. If M takes other values, especially for $M = 3$ (see the Appendix), except when $m_j = 0$, $2qm_j \pi/M = 2\pi/3$, or $4\pi/3$ modulo 2π , thus only partial interference can be expected.

For systems with additional mirror symmetry, there would appear periodic orbits that also have the same mirror symmetry, or if not, there would accompany another set of periodic orbits that is mirror symmetric to this one. The analysis of constructive or destructive interference would be similar as to that without mirror symmetries.

VII. CONCLUSIONS

To conclude, we have investigated a quantum billiard with fourfold rotational symmetry, whose classical dynamics are chaotic. The Hamiltonian can be reduced into four independent blocks with rotational quantum number $m = 0, 1, 2, 3$. Alternatively, the system can be regarded as a quantum billiard on the FD ($\theta \in [\theta_0, \theta_0 + \pi/2]$) of the original billiard region, with further constrains of the wave function on the symmetry lines θ_0 and $(\theta_0 + \pi/2)$: $\psi^{(m)}(\theta_0 + \pi/2) = \exp(im\pi/2)\psi^{(m)}(\theta_0)$. The eigenvalues of the $m = 1$ and $m = 3$ symmetry subspaces degenerate, and the corresponding eigenwave functions are complex conjugates for each other. Depending on the types of FDOs, the states along these orbits can interfere constructively or destructively, leading to either enhancement or cancellation of the peaks in the length spectra plot. The advantage of the fourfold rotational symmetry quantum billiard over that of the threefold case is that here, when combining energy levels from different symmetry subgroups, for some peaks, they may cancel completely. We have carried out extensive numerical calculations to yield a large number of eigenenergies and eigenstates with high precision. The length spectra indeed show complex behaviors in terms of interference. We have also carried out detailed analysis of the phase accumulation for both forward and backward orientations on the FDOs, and obtained explicit expressions of the phase difference, which is the key to determine the interference. The analysis explains the appearance and disappearance of the peaks in the length spectra perfectly.

The constructive or destructive interference that we have analyzed in this work could be observed experimentally using superconducting microwave billiards, where eigenfrequencies (eigenenergies) belonging to different symmetry subspaces can be distinguished by splitting doublets and different responses to the phase perturbations. Therefore, the length spectra analysis using only the energy levels belonging to one symmetry subspace becomes meaningful and may render possible applications due to the discrete symmetries.

ACKNOWLEDGMENTS

We thank Dr. Chengzhen Wang and Prof. M. Du, Prof. B. Dietz, and Prof. Y.-C. Lai for illuminating discussions. This work was supported by NSFC under Grants No. 11775101 and No. 11422541.

APPENDIX: RESULTS FOR A THREEFOLD ROTATIONAL SYMMETRY QUANTUM BILLIARD

For the threefold rotational symmetry billiard, we construct with the following equation:

$$w = [z(1 + 0.1 \times z^3 + i \times 0.1 \times z^6)] \times R, \quad (\text{A1})$$

where

$$z = \rho \exp(i\phi), \quad \rho \in [0, 1] \text{ and } \phi \in [0, 2\pi].$$

Such a region keeps the threefold rotational symmetry but no mirror symmetry, and the classical dynamics have been confirmed to be chaotic. Level statistics for different symmetry subspaces are also checked, which is GOE for $m = 0$ and GUE for $m = 1$ (or $m = -1$ as these two subspaces have degenerate eigenenergies), consistent with previous results [24–28].

As shown in Fig. 7, the shortest FDOs in this billiard are the one third of those regular triangles. The length spectra peaks of the FDOs are partially canceled. The relative height of the peaks can be understood as follows.

Similar to the square orbits of the fourfold rotational symmetry case discussed in Sec. III A of the main text, e.g., Eqs. (17)–(22), we have for the forward direction (“+,” $A - B - A$) FDOs shown in Fig. 7:

$$\begin{aligned} \tilde{\psi}_j^{(m)}|_A &= \exp(-im2\pi/3) \exp\left[i\left(kl + \frac{\pi}{2}\right)\right] \psi_j^{(m)}|_A \\ &= \exp(i\Phi^+) \psi_j^{(m)}|_A, \end{aligned} \quad (\text{A2})$$

with

$$\Phi^+ = -m2\pi/3 + \left(kl + \frac{\pi}{2}\right). \quad (\text{A3})$$

For backward direction (“-,” $B - A - B$), we have

$$\begin{aligned} \tilde{\psi}_j^{(m)}|_B &= \exp(im2\pi/3) \exp\left[i\left(kl + \frac{\pi}{2}\right)\right] \psi_j^{(m)}|_B \\ &= \exp(i\Phi^-) \psi_j^{(m)}|_B, \end{aligned} \quad (\text{A4})$$

thus

$$\Phi^- = m2\pi/3 + \left(kl + \frac{\pi}{2}\right). \quad (\text{A5})$$

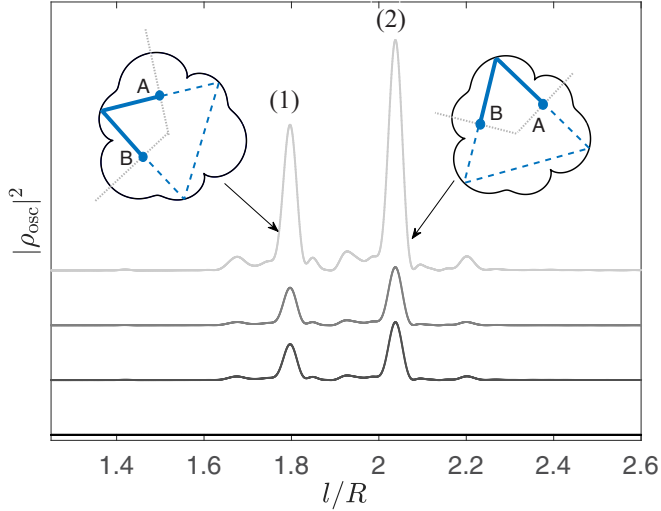


FIG. 7. From top to bottom, the four curves are the length spectra for energy levels belonging to the symmetry subspace $m = 0$, $m = 1$, the mixture of the two symmetry subspaces $m = 0$ and $m = 1$, and the mixture of all the three symmetry subspaces. The whole length L of the regular triangular orbit corresponding to peak (1) is $5.393R$ and the FDO's length is $l = L/3$. Similarly, the whole length of the orbit corresponding to peak (2) is $6.113R$ and the FDO's length is $l = L/3$.

Denote $A^\pm(l)$ as the contribution to the length spectra from states with forward and backward orientation, then we have

$$A^+(l) = e^{i\Delta\Phi} A^-(l), \quad (\text{A6})$$

where $\Delta\Phi = \Phi^+ - \Phi^- = -m4\pi/3$.

The height of the peak in the length spectrum at length l is

$$\begin{aligned} \rho_{\text{osc}}(l)^2 &\sim |A^+(l) + A^-(l)|^2 \\ &= |1 + e^{-im4\pi/3}|^2 |A^-(l)|^2. \end{aligned} \quad (\text{A7})$$

For the symmetry subspace $m = 0$, one has

$$\rho_{\text{osc}}(l)^2 \sim 4|A^-(l)|^2, \quad (\text{A8})$$

thus the two orientations interfere constructively. For the symmetry subspace $m = 1$, one has

$$\begin{aligned} \rho_{\text{osc}}(l)^2 &\sim |1 + e^{-i4\pi/3}|^2 |A^-(l)|^2 \\ &= |e^{i\pi/3}|^2 |A^-(l)|^2 = |A^-(l)|^2, \end{aligned} \quad (\text{A9})$$

the interference between the two orientation is partially destructive, resulting in a height that is the same when only one orientation is present. Thus, the height of the peaks for the symmetry subspace $m = 0$ is four times as that for $m = 1$, which can be seen from Fig. 7.

When combining the two symmetry subspaces together, we have

$$\begin{aligned} \rho_{\text{osc}}(l)^2 &\sim |A_{(m=0)}^+ + A_{(m=0)}^- + A_{(m=1)}^+ + A_{(m=1)}^-|^2 \\ &\sim |1 + 1 + e^{-i2\pi/3} + e^{i2\pi/3}|^2 |A^\pm(l)|^2 = |A^\pm(l)|^2. \end{aligned}$$

Therefore, due to the partially destructive interference, the height of the peak for the FDO shown in Fig. 7 when combining the two symmetry subspaces together is the same as that for the single symmetry subspace $m = 1$, and is one-fourth of that for $m = 0$. Only when combining all the three symmetry subspaces,

$$\begin{aligned} \rho_{\text{osc}}(l)^2 &\sim |A_{(m=0)}^+ + A_{(m=0)}^- + A_{(m=1)}^+ \\ &\quad + A_{(m=1)}^- + A_{(m=-1)}^+ + A_{(m=-1)}^-|^2 \\ &\sim |1 + 1 + e^{-i2\pi/3} + e^{i2\pi/3} \\ &\quad + e^{i2\pi/3} + e^{-i2\pi/3}|^2 |A^\pm(l)|^2 \\ &= 0, \end{aligned}$$

the interference destructs completely, and the peaks disappear.

-
- [1] P. Cvitanović and B. Eckhardt, *Nonlinearity* **6**, 277 (1993).
 [2] O. Bohigas, M. J. Giannoni, and C. Schmit, *Phys. Rev. Lett.* **52**, 1 (1984).
 [3] A. V. Andreev, O. Agam, B. D. Simons, and B. L. Altshuler, *Phys. Rev. Lett.* **76**, 3947 (1996).
 [4] T. Guhr, A. M. Groeling, and H. A. Weidenmüller, *Phys. Rep.* **299**, 189 (1998).
 [5] M. L. Mehta and E. P. Wigner, Review of ‘random matrices and the statistical theory of energy levels’, in *Historical and Biographical Reflections and Syntheses*, edited by J. Mehra (Springer, Berlin/Heidelberg, 2001), pp. 506–507.
 [6] M. V. Berry and M. Robnik, *J. Phys. A: Math. Gen.* **19**, 649 (1986).
 [7] P. So, S. M. Anlage, E. Ott, and R. N. Oerter, *Phys. Rev. Lett.* **74**, 2662 (1995).
 [8] U. Stoffregen, J. Stein, H. J. Stöckmann, M. Kús, and F. Haake, *Phys. Rev. Lett.* **74**, 2666 (1995).
 [9] B. Dietz, T. Friedrich, H. L. Harney, M. Miski-Oglu, A. Richter, F. Schäfer, and H. A. Weidenmüller, *Phys. Rev. Lett.* **98**, 074103 (2007).
 [10] B. Dietz, H. L. Harney, O. N. Kirillov, M. Miski-Oglu, A. Richter, and F. Schäfer, *Phys. Rev. Lett.* **106**, 150403 (2011).
 [11] S. Bittner, B. Dietz, U. Günther, H. L. Harney, M. Miski-Oglu, A. Richter, and F. Schäfer, *Phys. Rev. Lett.* **108**, 024101 (2012).
 [12] B. Dietz, T. Klaus, M. Miski-Oglu, A. Richter, and M. Wunderle, *Phys. Rev. Lett.* **123**, 174101 (2019).
 [13] M. V. Berry and R. Mondragon, *Proc. R. Soc. Lond. A: Math. Phys. Eng. Sci.* **412**, 53 (1987).
 [14] H. Y. Xu, L. Huang, Y.-C. Lai, and C. Grebogi, *Phys. Rev. Lett.* **110**, 064102 (2013).
 [15] C.-Z. Wang, L. Huang, and K. Chang, *New J. Phys.* **19**, 013018 (2017).
 [16] M.-Y. Song, Z.-Y. Li, H.-Y. Xu, L. Huang, and Y.-C. Lai, *Phys. Rev. Res.* **1**, 033008 (2019).
 [17] L. Huang, H.-Y. Xu, Y.-C. Lai, and C. Grebogi, *Chinese Phys. B* **23**, 070507 (2014).
 [18] L. Huang, H.-Y. Xu, C. Grebogi, and Y.-C. Lai, *Phys. Rep.* **753**, 1 (2018).
 [19] B. Gutkin, *J. Phys. A: Math. Theor.* **40**, F761 (2007).
 [20] G. Veble, T. Prosen, and M. Robnik, *New J. Phys.* **9**, 15 (2007).

- [21] B. Gutkin, *Proc. Am. Math. Soc.* **137**, 2795 (2009).
- [22] L. A. Bunimovich and G. D. Magno, *Commun. Math. Phys.* **288**, 699 (2009).
- [23] B. Dietz, T. Guhr, B. Gutkin, M. Miski-Oglu, and A. Richter, *Phys. Rev. E* **90**, 022903 (2014).
- [24] F. Leyvraz, C. Schmit, and T. H. Seligman, *J. Phys. A: Math. Gen.* **29**, L575 (1996).
- [25] C. Dembowski, H. D. Gräf, A. Heine, H. Rehfeld, A. Richter, and C. Schmit, *Phys. Rev. E* **62**, R4516 (2000).
- [26] R. Schäfer, M. Barth, F. Leyvraz, M. Müller, T. H. Seligman, and H.-J. Stöckmann, *Phys. Rev. E* **66**, 016202 (2002).
- [27] C. Dembowski, B. Dietz, H. D. Gräf, A. Heine, F. Leyvraz, M. Miski-Oglu, A. Richter, and T. H. Seligman, *Phys. Rev. Lett.* **90**, 014102 (2003).
- [28] C. H. Joyner, S. Müller, and M. M. A. Sieber, *J. Phys. A: Math. Theor.* **45**, 205102 (2012).
- [29] M. C. Gutzwiller, *J. Math. Phys.* **8**, 1979 (1967).
- [30] M. C. Gutzwiller, *J. Math. Phys.* **10**, 1004 (1969).
- [31] M. C. Gutzwiller, *J. Math. Phys.* **11**, 1791 (1970).
- [32] M. C. Gutzwiller, *J. Math. Phys.* **12**, 343 (1971).
- [33] R. Balian and C. Bloch, *Ann. Phys.* **85**, 514 (1974).
- [34] M. Berry, in *Les Houches Lecture Series Session XXXVI*, edited by G. Iooss, R. H. G. Helleman, and R. Stora (North Holland, Amsterdam, 1983), pp. 171–271.
- [35] J. M. Robbins, *Phys. Rev. A* **40**, 2128 (1989).
- [36] B. Lauritzen, *Phys. Rev. A* **43**, 603 (1991).
- [37] T. H. Seligman and H. A. Weidenmüller, *J. Phys. A: Math. Gen.* **27**, 7915 (1994).
- [38] J. P. Keating and J. Robbins, *J. Phys. A: Math. Gen.* **30**, L177 (1997).
- [39] S. W. McDonald and A. N. Kaufman, *Phys. Rev. Lett.* **42**, 1189 (1979).
- [40] S. W. McDonald and A. N. Kaufman, *Phys. Rev. A* **37**, 3067 (1988).
- [41] E. J. Heller, *Phys. Rev. Lett.* **53**, 1515 (1984).
- [42] L. Huang, Y.-C. Lai, D. K. Ferry, S. M. Goodnick, and R. Akis, *Phys. Rev. Lett.* **103**, 054101 (2009).
- [43] X. Ni, L. Huang, Y.-C. Lai, and C. Grebogi, *Phys. Rev. E* **86**, 016702 (2012).
- [44] D. J. Mason, M. F. Borunda, and E. J. Heller, *Phys. Rev. B* **88**, 165421 (2013).
- [45] D. Cabosart, A. Felten, N. Reckinger, A. Iordanescu, S. Toussaint, S. Faniel, and B. Hackens, *Nano Lett.* **17**, 1344 (2017).
- [46] P. J. J. Luukko, B. Drury, A. Klales, L. Kaplan, E. J. Heller, and E. Räsänen, *Sci. Rep.* **6**, 37656 (2016).
- [47] J. Keski-Rahkonen, P. J. J. Luukko, L. Kaplan, E. J. Heller, and E. Räsänen, *Phys. Rev. B* **96**, 094204 (2017).
- [48] J. Keski-Rahkonen, A. Ruhanen, E. J. Heller, and E. Räsänen, *Phys. Rev. Lett.* **123**, 214101 (2019).
- [49] J. Keski-Rahkonen, P. J. J. Luukko, S. Åberg, and E. Räsänen, *J. Phys. Cond. Matt.* **31**, 105301 (2019).
- [50] C. J. Turner, A. A. Michailidis, D. A. Abanin, M. Serbyn, and Z. Papić, *Nat. Phys.* **14**, 1 (2018).
- [51] S. Moudgalya, N. Regnault, and B. A. Bernevig, *Phys. Rev. B* **98**, 235156 (2018).
- [52] W. W. Ho, S. Choi, H. Pichler, and M. D. Lukin, *Phys. Rev. Lett.* **122**, 040603 (2019).
- [53] S. Choi, C. J. Turner, H. Pichler, W. W. Ho, A. A. Michailidis, Z. Papić, M. Serbyn, M. D. Lukin, and D. A. Abanin, *Phys. Rev. Lett.* **122**, 220603 (2019).
- [54] C.-J. Lin and O. I. Motrunich, *Phys. Rev. Lett.* **122**, 173401 (2019).
- [55] M. Schechter and T. Iadecola, *Phys. Rev. Lett.* **123**, 147201 (2019).
- [56] T. Iadecola, M. Schechter, and S. Xu, *Phys. Rev. B* **100**, 184312 (2019).
- [57] R. W. Robinett, *J. Math. Phys.* **40**, 101 (1999).
- [58] M. Robnik, *J. Phys. A: Math. Gen.* **17**, 1049 (1984).
- [59] T. Prosen and M. Robnik, *J. Phys. A: Math. Gen.* **26**, 2371 (1993).
- [60] O. Bohigas, D. Boosé, R. E. De Carvalho, and V. Marvulle, *Nucl. Phys. A* **560**, 197 (1993).
- [61] H.-J. Stöckmann, *Quantum Chaos: An Introduction* (Cambridge University Press, New York, 2006).
- [62] F. Haake, *Quantum Signatures of Chaos*, 3rd ed., Springer series in synergetics (Springer-Verlag, Berlin, 2010).
- [63] H.-J. Stöckmann and J. Stein, *Phys. Rev. Lett.* **64**, 2215 (1990).
- [64] E. G. Vergini, *Phys. Rev. Lett.* **108**, 264101 (2012).
- [65] E. G. Vergini, *Europhys. Lett.* **110**, 10010 (2015).